

## ***In situ* characterization of vapor phase growth of iron oxide-silica nanocomposites: Part I. 2-D planar laser-induced fluorescence and Mie imaging**

Brian K. McMillin<sup>a)</sup>

*Chemical Science and Technology Laboratory, National Institute of Standards and Technology, Gaithersburg, Maryland 20899-0001*

Pratim Biswas<sup>b)</sup>

*Aerosol and Air Quality Research Laboratory, Department of Environmental Engineering, University of Cincinnati, Cincinnati, Ohio 45221-0071*

Michael R. Zachariah<sup>c)</sup>

*Chemical Science and Technology Laboratory, National Institute of Standards and Technology, Gaithersburg, Maryland 20899-0001*

(Received 3 April 1995; accepted 3 January 1996)

Planar laser-based imaging measurements of fluorescence and particle scattering have been obtained during flame synthesis of iron-oxide/silica superparamagnetic nanocomposites. The theory and application of laser-induced fluorescence, the spectroscopy of FeO(g), and the experimental approach for measurement of gas phase precursors to particle formation are discussed. The results show that the vapor phase FeO concentration rapidly rises at the primary reaction front of the flame and is very sensitive to the amount of precursor added, suggesting nucleation-controlled particle growth. The FeO vapor concentration in the main nucleation zone was found to be insensitive to the amount of silicon precursor injected, indicating that nucleation occurred independently for the iron and silicon components. Light scattering measurements indicate that nanocomposite particles sinter faster than single component silica, in agreement with TEM measurements.

### **I. INTRODUCTION**

An area of current interest in materials processing is the synthesis of structures on an atomic to nanometer scale. Particles with dimensions of less than 100 nm are referred to as "nanoparticles," and these nanophase materials possess unique advantages with respect to their processing and, more importantly, their properties.<sup>1-4</sup> Flame aerosol reactors offer a potential route for the production of large quantities of nanostructured materials,<sup>5</sup> but at present the formation and nucleation of nanophase particles from the gas phase are not well understood. Developing a better understanding of the gas phase chemistry is important, though, because the chemistry and interaction of the gas phase precursors in this high temperature environment are critical in establishing the final particle characteristics (sizes and chemical composition).

*In situ* measurements aimed at investigating the gas phase species' concentrations, temperature field, and

particle size and distributions are therefore of great interest, because they can lead to a better understanding of the underlying chemical/transport phenomena that occur during particle synthesis. While conventional diagnostic tools such as thermocouples and mass/particle sampling probes have been used in the past, laser-based diagnostics offer nonintrusive, sensitive techniques for measuring particle size/number density, gas temperature, and species concentration in these reactors. For example, laser-based Rayleigh/Mie scattering has been used for measuring particle size and number density in both aerosol and combustion research applications (see, for example, Ref. 6). *In situ* multiphoton ionization for gas phase species detection has been demonstrated even in particle laden flows.<sup>7</sup> Laser-induced fluorescence (LIF) has also been used extensively for gas phase concentration and temperature in combustion flows<sup>8</sup> and, to a lesser extent, in low pressure plasma processing reactors,<sup>9</sup> but it has not found application in aerosol research. One of the few applications of LIF in particle synthesis work is that reported by Zachariah and Burgess<sup>10</sup> where they used LIF to measure OH and SiO concentrations, and Mie scattering to measure particle distributions during flame synthesis of silica. Mie scat-

<sup>a)</sup>National Research Council/NIST postdoctoral fellow.

<sup>b)</sup>Work performed while on sabbatical at NIST.

<sup>c)</sup>Author to whom correspondence should be addressed.

tering measurements in a similar application have also been reported by Zachariah *et al.*<sup>11,12</sup> and Chang and Biswas.<sup>13</sup>

While laser-based measurements have proven to be effective in a number of investigations of chemically reacting flows, the majority of previous measurements have been limited to one-dimensional profiling based on single-point techniques. Recently, a number of experiments in the combustion research community have extended these techniques to two-dimensional, i.e., planar laser-induced fluorescence (PLIF) imaging and planar Rayleigh/Mie scattering measurements.<sup>14,15</sup> In these two-dimensional measurements, a thin sheet of laser light is used to illuminate the flow and the resulting signal is collected with a lens and imaged onto a sensitive CCD camera. In addition to providing efficient data collection, these planar imaging measurements are useful because they provide a means to simultaneously measure flow properties and visualize flow structures in two dimensions, with excellent spatial resolution.

The purpose of this paper is to demonstrate the application of planar laser-based imaging measurements in a particle synthesis flame reactor, and to examine, through *in situ* chemical species measurement, the general features of multicomponent particle formation. In this paper, we describe two-dimensional imaging of gas phase ferrous oxide (FeO) fluorescence and Rayleigh/Mie particle scattering obtained during flame synthesis of nanoscale iron oxide/silica particles. These nanocomposite particles, composed of magnetic  $\gamma$ -Fe<sub>2</sub>O<sub>3</sub>/Fe<sub>3</sub>O<sub>4</sub> encapsulated in a silica matrix, have recently been synthesized in flames and, in displaying superparamagnetism, may have potential impact in magnetic refrigeration technology.<sup>16</sup> Several other materials of interest consist of more than one component and are made from multiple precursors as well,<sup>5</sup> including high temperature superconducting ceramics,<sup>17–21</sup> optical fiber preforms,<sup>22</sup> magnetic materials,<sup>23</sup> and optical ceramics.<sup>25</sup>

In the sections that follow, we briefly review the theory and application of LIF, discuss the spectroscopy of FeO, and describe the experimental setup and procedure. We then present experimental results, which include images of the gas phase FeO concentration and of particle scattering throughout the flame at various conditions. In part II of the paper, experimental data are compared to predictions of a discrete sectional aerosol model accounting for the gas phase reaction and nucleation kinetics.

## II. PLIF TECHNIQUE

### A. Basic theory

The theory and application of laser-induced fluorescence (PLIF) and particle scattering have been described

in detail elsewhere (see, for example, Refs. 8, 14, 26, and 27), so we will only briefly review the PLIF technique. PLIF is a well-established spectroscopic flow diagnostic, based on monitoring the spontaneous radiative emission (fluorescence) following absorption of laser photons by a species present within a flowfield. In a typical PLIF experiment, a thin sheet of frequency-tuned, pulsed laser light is used as the excitation source. The laser sheet is directed through the flow and the resulting broadband fluorescence from the illuminated region is imaged with a lens onto an intensified, charge-coupled device (CCD) camera. Through various excitation and detection strategies, the pulse-integrated fluorescence signal can be related to certain flow properties, such as the absorbing species concentration and gas temperature. In many cases only relative measurements are obtained, but in principal, absolute measurements of concentration and/or temperature can be determined either through calibration or an additional independent measurement at some point within the imaged region.

Assuming weak laser excitation and a spectrally broad laser with respect to the absorption linewidth, the temporally integrated fluorescence signal,  $S_f$ , can be modeled by

$$S_f \propto EN_{\text{abs}}F_B(T) \frac{A}{A + Q}, \quad (1)$$

where  $N_{\text{abs}}$  is the absorbing species number density,  $F_B(T)$  is the Boltzmann population fraction of the absorbing state at temperature  $T$ ,  $A$  is the Einstein coefficient of spontaneous emission,  $E$  is the laser energy, and  $Q$  is the collisional quenching rate coefficient, which depends upon the local chemical composition, number density, and temperature. The term  $A/(A + Q)$  is the fluorescence efficiency and represents the fraction of laser-excited molecules which fluoresce, rather than collisionally relax to the ground electronic state.

As Eq. (1) illustrates, determining the absorbing species concentration from the fluorescence signal generally requires knowledge of the local collisional quenching rate coefficient and temperature. Indeed, accounting for the collisional quenching is typically the most difficult aspect of relating the fluorescence signal to the absorbing species concentration. Several approaches have been used in previous studies to account for quenching in linear fluorescence measurements (for a more detailed discussion which also includes saturated fluorescence measurements, see Ref. 8). For example, the quenching rate can be determined experimentally by monitoring the fluorescence decay, but this approach is generally only used at low pressures, because in flows at atmospheric pressure and above, it usually requires subnanosecond time resolution.

Alternatively, the collisional quenching can be modeled using  $Q = N \cdot \sigma \langle v \rangle$ , where  $\sigma$  is a mixture-

averaged quenching cross-section and  $\langle v \rangle$  is the mean molecular speed. This approach is most useful where the temperature is known and the quenching is dominated by species whose cross sections and concentrations are known or can be reasonably estimated. Collisional quenching cross sections have been measured for a number of primary combustion species,<sup>8</sup> but limited data are available for other species. In cases where the cross sections or major species concentrations are not known, one can assume a given temperature dependence for  $\sigma$ . For example, assume  $Q \gg A$  (which is generally true in atmospheric pressure flames) and  $\sigma = \text{constant}$ , Eq. (1) reduces to  $S_f \propto N_{\text{abs}} F_B(T) / \sqrt{T}$ .<sup>15</sup> Finally, we note that the simplest approach is to assume that the quenching rate is essentially constant over a limited region or range of conditions. Under this assumption, Eq. (1) simplifies to  $S_f \propto N_{\text{abs}} \cdot F_B(T)$ , and, thus, the fluorescence signal depends only on absorbing species concentration and temperature. Although only approximately true at best, in several flame measurements the quenching rate has been found to be relatively constant over a limited range of conditions.<sup>8</sup> Hence, depending upon the accuracy needed, one might reasonably neglect variations in quenching in certain situations.

Using one of these strategies to account for the quenching, one can then use the fluorescence signal to determine the absorbing species concentration, provided some knowledge of the temperature or choice, if possible, of an absorption transition which minimizes the overall temperature dependence of the signal. Because no quenching data for FeO fluorescence is available, we assumed a constant value through the flame, and, as discussed below, chose a transition whose initial quantum state population fraction,  $F_B(T)$ , was relatively constant over the temperature range of interest. Subject to these approximations, the fluorescence signal was used as a direct measure of the relative FeO concentration throughout the flame.

## B. FeO spectroscopy

The spectroscopy of FeO is exceptionally complicated for a diatomic molecule and, to date, is not completely understood. Based on the analyses of Cheung *et al.*<sup>28</sup> and Harris and Barrow,<sup>29</sup> we briefly describe details of FeO spectroscopy that are relevant to these measurements. For a more complete discussion on spectroscopy and its notation in general, the reader is referred to Herzberg.<sup>30</sup>

The laser-induced fluorescence excitation and detection scheme used for these measurements is shown schematically in Fig. 1, which shows a partial energy level diagram for the FeO molecule. In the figure, the  $v'' = 0, 1, 2,$  and  $3$  vibrational levels of the  $X^5\Delta_4$  ground electronic is shown, as is the  $v' = 0$  vibrational level of

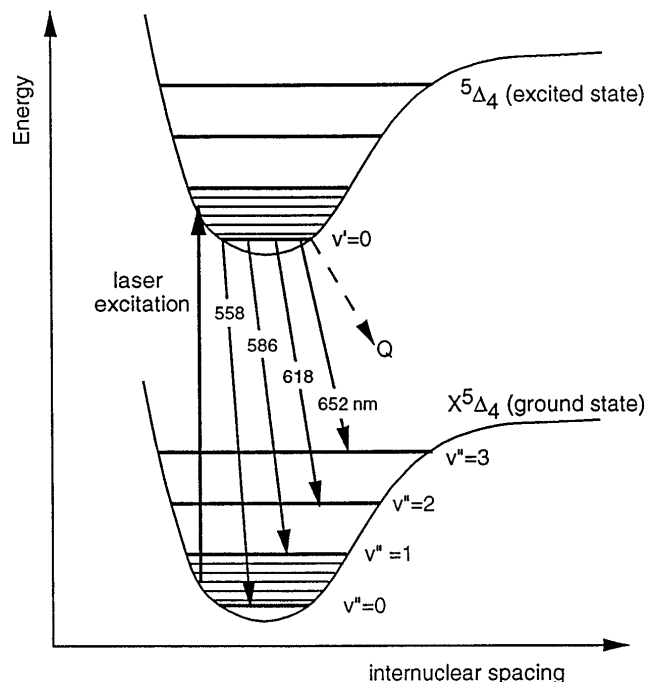


FIG. 1. Partial energy level diagram for FeO showing the excitation and detection scheme used in this study.

the  $^5\Delta_4$  excited electronic state. Each vibrational level also contains a manifold of rotational levels, which are shown schematically for only the lowest vibrational level in each electronic state. As denoted by the upward-pointing arrow, the laser was tuned to excite transitions between a particular rotational level within the  $X^5\Delta_4$   $v'' = 0$  level and a rotational level within the electronically excited  $^5\Delta_4$   $v' = 0$  level.

Following laser excitation, molecules within the upper electronic state can either radiatively or nonradiatively decay (i.e., fluoresce or quench) to various lower states, as depicted by the downward-pointing arrows. In the figure, the fluorescence is denoted by the solid downward arrows, and the quenching is denoted by the dashed downward arrow. Since collisional transfer can redistribute the excited molecules throughout the rotational manifold, the spontaneous emission and collisional quenching processes are shown originating from the entire manifold rather than just the upper laser-coupled state. While spontaneous emission to other lower states may also occur, the majority of the laser-induced fluorescence of FeO in the present experiments is emitted over the wavelength range of 558–652 nm, as indicated in the figure. This particular excitation/detection scheme was selected because the absorption transitions occur in a relatively simple region of the complex FeO spectrum, and because the fluorescence was known to occur both at wavelengths (essentially) resonant with the laser ( $\sim 558$  nm), and at longer, nonresonant wavelengths (586–652 nm).

Using an excitation/detection strategy that provides reasonably strong nonresonant fluorescence was a requirement for these measurements, so that the intense laser scattering from particles could be spectrally filtered from the measured fluorescence signal (see Ref. 10 for more detailed discussion of this point). In the fluorescence measurements reported here, spectral filtering was also used to suppress the particle luminosity from reaching the camera, at wavelengths outside of the primary fluorescence wavelength region (for additional details, see Sec. III below). Although necessary to avoid corrupting the fluorescence signal with extraneous noise, this spectral filtering also resulted in some loss in the collection efficiency of the fluorescence. Specifically, the long-pass filter used for blocking the laser scattering also unavoidably blocked the FeO (resonant) fluorescence band near 558 nm, and reduced the fluorescence signal accordingly. Indeed, based on FeO LIF dispersion measurements using a monochromator and photomultiplier tube, we determined that a significant fraction of the fluorescence signal (50% or more) was sacrificed through filtering the laser scattering. In contrast, though, the 650 nm short-pass filter, used to suppress intense particle luminosity, caused only a minor reduction in the detected fluorescence signal.

Figure 2 shows a partial laser excitation spectrum of the FeO near 448 nm. This spectrum was recorded by directing the laser beam through a methane-oxygen-iron carbonyl flame, scanning the laser from 558.5 to 561.0 nm, and monitoring the fluorescence bands near 586 and 618 nm using a photomultiplier tube and boxcar averager. Noted in the figure and assigned based on the line positions tabulated by Harris and Barrow,<sup>29</sup> the transition used for these fluorescence imaging measurements was the overlapping  $P(17) + R(40)$  line pair in the  ${}^5\Delta_4 \leftarrow X^5\Delta_4$  (0,0) orange system of FeO. This transition pair was chosen because it provided the most signal among the isolated transitions, and because it exhibits a reasonable temperature-independent signal over the range of interest.

The expected temperature dependence of the fluorescence signal is illustrated in Fig. 3, which shows a plot of the combined Boltzmann population fractions of the two initial states excited by the laser. Over the temperature range of interest here (1800–2400 K), the net population fraction of the two initial states varies by  $\pm 25\%$ , and exhibits a monotonic decrease from low to high temperatures. In calculating the initial states' net Boltzmann fraction as a function of temperature, we included the contributions of the rotational, vibrational, and electronic partition functions, using the term energies reported by Cheung *et al.*<sup>31</sup> and the procedure outlined by Tatum.<sup>32</sup> In contrast to many diatomic flame species, for FeO there are a number of low-lying vibrational and electronic states that are well populated at flame

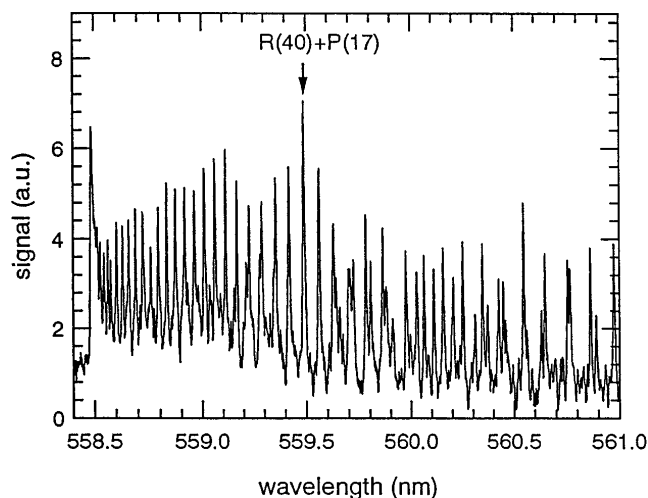


FIG. 2. Laser excitations spectrum of FeO near 558 nm.

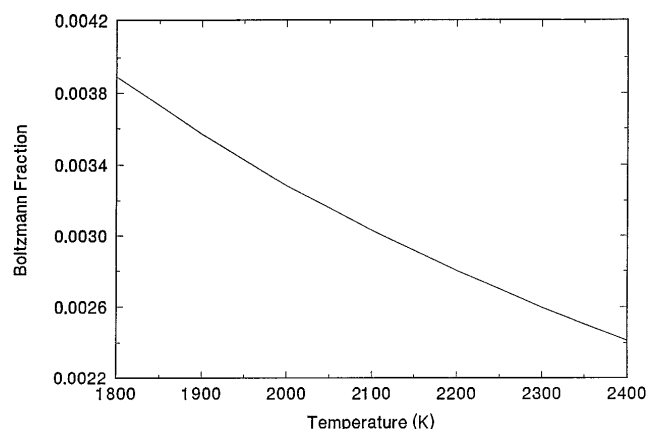


FIG. 3. Expected temperature dependence of the fluorescence signal based on the calculated variation of the two initial states' Boltzmann fraction with temperature.

temperatures. Hence, the temperature dependence of the Boltzmann fraction in Fig. 3 results from variations in the vibrational, rotational, and electronic state populations, in order of decreasing importance.

### III. EXPERIMENTAL DETAILS

#### A. Flame synthesis

The experiments were conducted using a water-cooled premixed burner mounted on a vertical translation stage. As summarized in Table I, methane/oxygen flames, diluted with nitrogen and seeded with iron and/or silicon bearing precursors, were investigated. The precursors used were iron carbonyl and hexamethyldisiloxane which are liquids at room temperature. These precursors were delivered (from a bubbler at 20 °C) as saturated vapors in argon and introduced into a mixing manifold upstream of the reactor.

A premixed flame operating at high temperature was used to create an environment thermodynamically favoring the desired particle structure (see a discussion of this point in Zachariah *et al.*<sup>16</sup>), and to provide optical access for examination of potential precursor decomposition prior to the flame zone. By design, this configuration ensures that the precursors rapidly reach a high temperature ( $>2000$  K) wherein they decompose and form their respective oxides. Particles could then be extracted by rapid quenching to minimize the formation of  $\text{Fe}_2\text{SiO}_4$ , which occurs below 1500 K.<sup>16</sup> In addition, an oxygen-rich flame stoichiometry was maintained to minimize undesired carbon contamination in the resulting particles. The basic features involved in the nanocomposite growth process are depicted in Fig. 4, and a more thorough discussion based on the results presented here will be discussed later in the body of this paper. The typical morphology of the particles produced are shown in Fig. 5 and discussed, along with chemical composition and magnetic properties, in a prior publication.<sup>16</sup>

## B. PLIF implementation

As shown in schematically in Fig. 6, the laser excitation source used for the optical measurements was an XeCl excimer-pumped dye laser, operating at 10 Hz with a  $\sim 30$  ns pulse duration,  $\sim 5$  mJ pulse energy, and  $\sim 0.2$   $\text{cm}^{-1}$  bandwidth. Using a cylindrical and spherical lens combination, the beam was expanded vertically, formed into a thin sheet, and directed through the center of the flame. Within the imaged region of the flame, the laser sheet measured  $\sim 300$   $\mu\text{m} \times 35$  mm. The laser energy and spatial distribution were monitored during the experiments by directing a 5% reflection of the

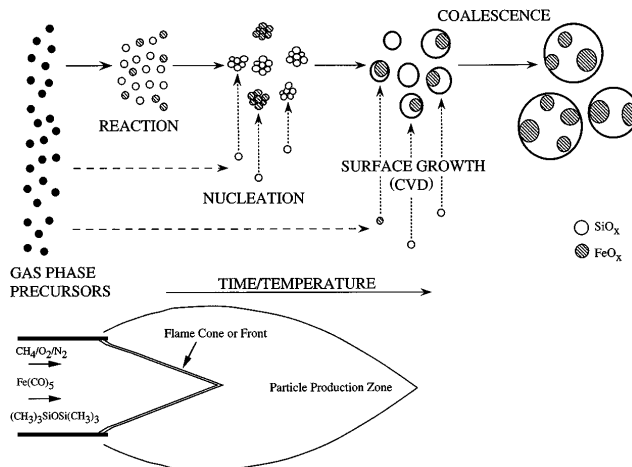


FIG. 4. Particle growth processes occurring.

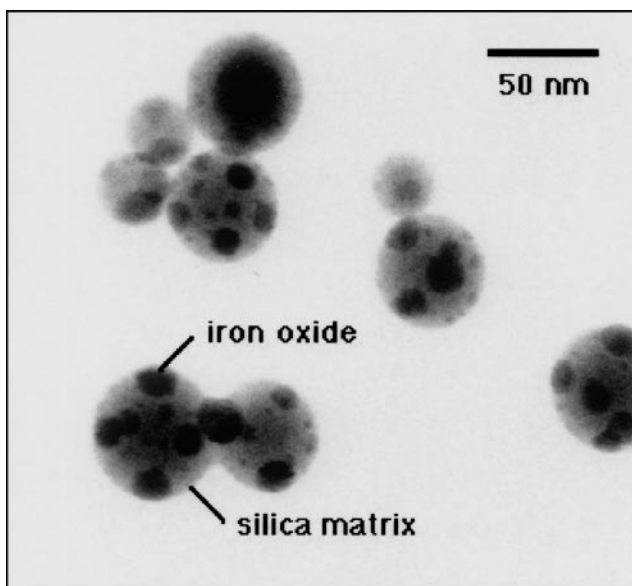


FIG. 5. TEM image of typical iron oxide/silica nanocomposite particles synthesized in these experiments.

TABLE I. Experimental conditions.

Reactants fraction	Flow rates (lpm @ 20 °C)	Mole		
Methane	0.93	0.11		
Oxygen	2.33	0.28		
Nitrogen	5.00	0.60		
Argon (iron carbonyl bubbler)	0.05, 0.14, 0.24			
Argon (Si bubbler)	0.14, 0.24			
Parametric tests				
Test no.	Precursor feed rates ( $10^{-6}$ moles/s)		LIF	Scattering
	Iron	Silicon		
1	1.06	...	X	X
2	3.09	...	X	X
3	5.10	...	X	X
4	...	3.47	...	X
5	...	5.73	...	X
6	3.09	3.47	X	X
7	3.09	5.73	X	X

laser sheet onto a static dye cell, and recording the resulting fluorescence with a video CCD camera and frame-grabber computer board. For the LIF measurements, the laser was tuned to  $\sim 559.5$  nm to excite the  $P(17) + R(40)$  transition in the  ${}^5\Delta_4 \leftarrow {}^5\Delta_4$  (0,0) orange system of FeO. For the particle scattering measurements, the laser was tuned to 530 nm, where no gas phase transitions exist.

For both the fluorescence and particle scattering measurements, the signal was collected at a right angle to the illumination plane and imaged onto an intensified, cooled CCD camera ( $576 \times 384$  pixels, each 23  $\mu\text{m}$  square) using an  $f/4.5$  lens. To suppress flame emission within the images, the intensifier was synchronized to, and gated on for  $\sim 75$  ns during, each laser pulse. For the fluorescence measurements, an OG590 Schott glass

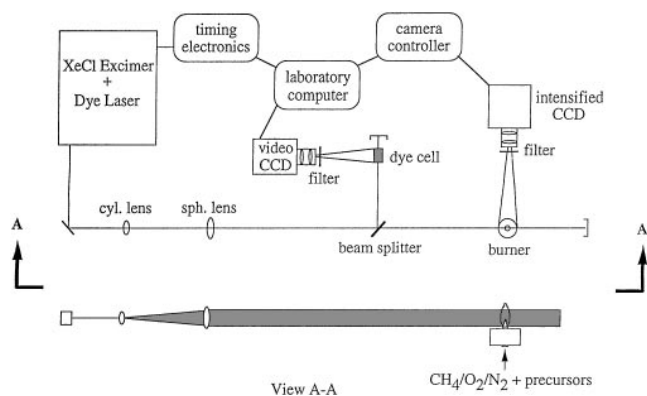


FIG. 6. Schematic diagram of the experimental setup.

(long-pass) filter was used to block laser scattering, and a Corion LS-650 short-pass filter was used to prevent flame luminosity, outside of the LIF wavelength region, from reaching the detector. For the particle scattering measurements, a Corion P10-530 line filter was used to suppress flame emission while passing the laser scattering. The images obtained were typically averaged over 250–300 laser shots to improve the signal-to-noise ratio, and were spatially averaged  $2 \times 2$  pixels, which is the effective resolution of the intensifier. While the resulting pixel resolution was  $\sim 150 \mu\text{m}$ , the effective spatial resolution of the measurements was  $\sim 300 \mu\text{m}$ , owing to the laser sheet thickness.

All of the images were corrected for camera dark background, flatfield uniform response of the camera and collection lens, and laser energy and spatial distribution. The fluorescence images were also corrected for laser-induced particle incandescence and scattering by subtracting images obtained with the laser detuned from the absorption transition. The flatfield correction was obtained by imaging uniform light from a standard, diffuse tungsten lamp, through the appropriate spectral filters for either FeO fluorescence or particle scattering. The video CCD images of laser-induced fluorescence from a static cell of dilute Rhodamine 590 laser dye in methanol were used to normalize the laser and vertical spatial distribution in the corrected images. The laser profile images were remapped from the video CCD to the intensified CCD coordinates based on images obtained with the laser sheet masked.

#### IV. RESULTS AND DISCUSSION

A series of experiments, summarized in Table I, were conducted to examine the mechanisms of Fe–Si–O particle formation in a premixed flame reactor. Two-dimensional images of FeO(g) LIF and particle scattering were obtained in flames seeded with just the iron precursor (cases 1, 2, and 3), and with both the iron and silicon precursors (cases 6 and 7). In addition, two-dimensional images of particle scattering were also obtained for

flames seeded with just the silicon precursor (cases 4 and 5). A discussion of the pertinent experimental results follows.

Figures 7(a)–7(c) show representative flame emission, FeO fluorescence, and Mie scattering images for experiments with an iron precursor feed (case 2), and Fig. 7(d) shows an additional scattering image for a flame seeded with both iron and silica precursors (case 7). Although not shown, the emission and FeO fluorescence images for flames seeded with both iron and silica precursors were qualitatively similar to Figs. 7(a) and 7(b), respectively. For cases with iron precursor feed, there is significant emission from the flame [Fig. 5(a)] due to the iron precursor oxidation products and black body emission from the particles. As mentioned previously, the gating of the intensifier and the use of the short pass filter (650 nm) were necessary to obtain reasonable fluorescence signal-to-background-emission ratios ( $>4:1$ ).

An FeO(g) LIF image of the flame region is shown in Fig. 7(b). While immediate decomposition is expected at the flame front, the low signal within the flame cone (see Fig. 4 for definition of flame cone) suggests that little decomposition occurs prior to the flame front. Downstream of the flame cone, the resultant high FeO(g) concentration regions are indicated by the dark blue regions in the figure. As the gases move away from the flame front, there is an onset of particle formation, and the FeO(g) concentration decreases downstream (indicated by the transition from blue to green to yellow to orange in the color map). The corresponding scattering image [Fig. 7(c)] reveals a central region wherein particle concentrations are low or the particles are too small to yield detectable signs (white region). Further downstream, an increase in the scattering signal is observed, consistent with the decreasing FeO(g) concentration. The scattering signal is highest near the radial boundary of the flame, presumably because particles are much larger there owing to faster nucleation rates resulting from the lower temperature, and the longer times available for growth by coagulation. It should also be noted that these images were time-averaged over 250 to 300 laser shots or approximately 2 min. Hence, particularly in the scattering images, the shear layer vortices (and flame flickering) contribute to the observed signal in the central downstream region of the flame, where the large particles from the radial boundary of the flame are carried toward the centerline by the flow.

Figure 7(d) shows a particle scattering image from a flame seeded with both iron and silicon precursors. Although not shown, scattering images for flames seeded with just the silicon precursor were qualitatively similar to that of Fig. 7(d). In comparing the two scattering images in Fig. 7, we find that the case with both silicon and iron precursors present is markedly different in two

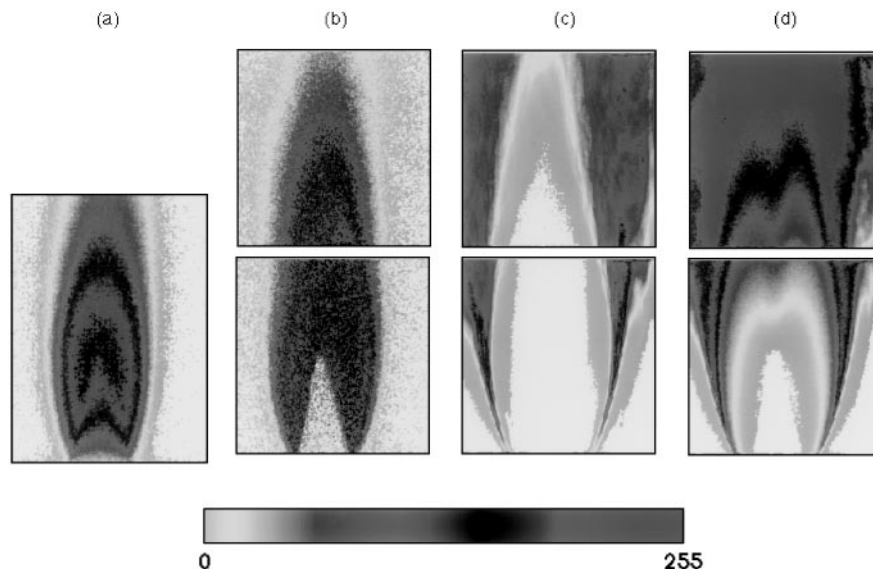


FIG. 7. Two-dimensional images of the flame including (a) chemiluminescent/blackbody emission, (b) LIF of FeO, (c) Mie scattering signal for conditions of case 2, and (d) Mie scattering signal for conditions of case 7. The LIF and scattering image show a region of the flame measuring approximately  $31 \times 31$  mm.

ways: (i) the scattering signals are generally much larger for the cases with silicon precursor present compared to those with only the iron precursor; and (ii) significant particle scattering is observed within the central region of the flame just above the cone tip, for cases with silicon precursor present. Interestingly, within the interior of the flame, we note that the scattering signal increases more rapidly along the centerline than along the streamlines just outside the centerline, leading to a scattering image with double-lobed isocontours resembling a smoothed letter “M”. We believe that the enhanced scattering signal along the center streamlines results from a slightly lower temperature as compared to adjacent, outer streamlines. The slightly lower temperature along the center streamlines would result in an increased nucleation rate with respect to the adjacent outer streamlines. Indeed, such a dip in the temperature distribution has been previously reported by Lewis and Von Elbe,<sup>33</sup> based on measurements of a lean methane/air flame in a rectangular burner. Although we cannot measure temperature with the accuracy of the Lewis and Von Elbe, our scattering image is very similar to their measured temperature contours and should be very sensitive to temperature.

While the two-dimensional images provide a great deal of information, examining the centerline profiles simplifies the comparison, since the flow is ideally one-dimensional along that streamline. Figure 8 shows the concentration of FeO(g) as a function of time (or axial position) for different inlet concentrations (cases 1, 2, and 3). The results are presented as a function of time from the flame front (distance from cone tip divided by local velocity), since the precursor decomposition

essentially begins at the conical flame front where the temperature rapidly increases. In this way, differences in the flame height occurring for different precursor concentrations can be removed to allow a better comparison.

As illustrated Fig. 8, the concentration of FeO(g) increases rapidly at the flame front, with a similar rate of increase for each precursor feed rate. This is followed by a decrease in the FeO(g) concentration due to the conversion of the vapor to the particle phase. The two processes of precursor oxidation [FeO(g) formation] and that of particle formation [FeO(g) consumption] take place simultaneously; however, the profiles indicate that the precursor oxidation is the faster of the two initially. This behavior is expected since one might approximate the FeO(g) formation rate to be (pseudo) first order with

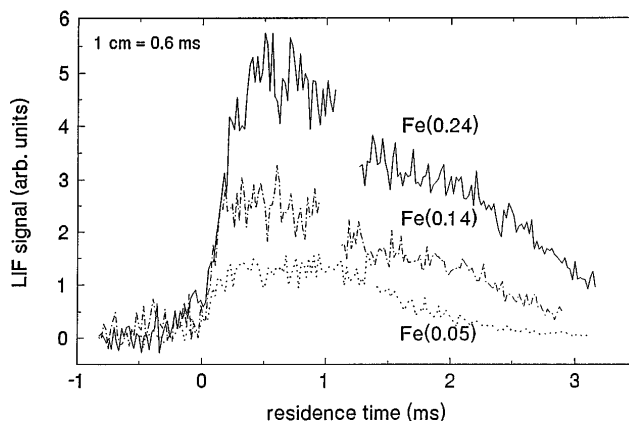


FIG. 8. Centerline profile of FeO(g) concentration as a function of time from the flame front for three different iron oxide precursor feed rates (cases 1, 2, and 3).

respect to the precursor concentration due to the excess oxygen, while the consumption (at least at early times) will be proportional to the square of the FeO(g) concentration resulting from FeO(g) dimerization. It should be pointed out that for these classes of materials, and temperatures used here, the vapor is typically in a highly supersaturated state and that the critical cluster size (using the terminology of classical nucleation theory) is less than a monomer. As such no thermodynamic barrier to nucleation exists, and one is basically dealing with a kinetically controlled process similar to any gas-phase chemical process. An analysis of this type has been performed by expressing the particle formation or nucleation rate as a kinetic process<sup>34-36</sup> with the rate proportional to the square of the concentration of FeO(g); thus, the drop-off in FeO(g) concentration is expected to be faster for the higher iron feed rates, and this is observed, to some extent, in Fig. 8.

An approximate temperature distribution in the flame region was measured using radiation ratio thermometry, and assuming conditions for grey body radiation over the ranges of temperature and wavelengths. Though a resolution, such as reported by Lewis and von Elbe,<sup>33</sup> was not obtained, the temperatures in the flame region were found to be 2200, 2360, and 2450 K for cases 1, 2, and 3, respectively.

Using the iron precursor feed rate for case 2 as a baseline condition, experiments were conducted with iron and two different silicon precursor feed conditions (cases 6 and 7). Representative centerline profiles for the FeO(g) relative concentration are shown in Fig. 9; for clarity results from only cases 2 and 7 are shown. In comparing the FeO(g) concentrations for cases with just iron and with both iron and silicon feeds, there is no significant difference in the initial rise in FeO concentration at the flame front. This is a particularly interesting and important result since it indicates that the chemistry of the iron precursor decomposition and subsequent nucleation are independent of the presence of the silicon chemistry and subsequent particle formation. Indeed, the flame configuration was originally chosen such that temperatures could be rapidly achieved and maintained ( $T > 2000$  K) which would ensure from thermodynamic phase equilibria considerations to distinct phases, iron oxide and silicon oxide rather than iron silicate.<sup>16</sup> The results show that the phase segregation occurs not only in the solid product collected, but in so far as we can tell, in the gas phase chemistry as well. Some differences are observed in the FeO vapor concentration at larger distances downstream, where the FeO(g) concentration seems to be slightly lower for the "iron and silicon" feed conditions. For the iron-only feed condition, the FeO vapor is converted to particles by homogenous nucleation. When both precursors are used, there is an additional pathway for transformation of FeO

vapor; that is, the silica particles provide an additional surface. This results in a slightly faster decrease in the FeO(g) concentrations as observed in Fig. 9. It should also be noted that this [condensations of FeO(g) onto silica particles] is probably a minor pathway, and the FeO(g) is primarily transformed directly to iron oxide particles. This is confirmed by the observation that increasing the silicon precursor concentration does not lead to significant change in the FeO(g) concentration profile (Fig. 9). Transmission electron microscopy (TEM) of the composite particles<sup>16</sup> indicated that the iron oxide particles are surrounded by a silica matrix, further confirming that distinct iron oxide particles are formed independently (see Fig. 4). A detailed comparison of quantitative contributions of each of these pathways will be discussed in a subsequent publication.

The centerline scattering profiles for cases 2-7 are shown in Fig. 10. In this figure, the data for cases 4-7 are from two-dimensional images, while the data for cases 2-3 (which are scaled by a factor of 100 in the figure) are based on photomultiplier tube measurements. A photomultiplier tube was used for cases 2-3 because of limitations on the dynamic range of the intensified CCD camera (at the gain required to detect particle scattering within the flame interior for cases 2-3, the intensifier could be locally damaged by the very large signals from the large particles on the flame boundary). To normalize the data for comparison, photomultiplier tube measurements of centerline scattering were also obtained for cases 6-7, and observed trends showed good agreement with the corresponding two-dimensional images.

For cases with only the iron precursor present (cases 2-3), the scattering signals are generally very low; however, there is a slight increase in the scattering signal with axial position, and generally higher signals with a higher feed rate, as expected. Much higher signals are obtained for the cases seeded exclusively with the silicon

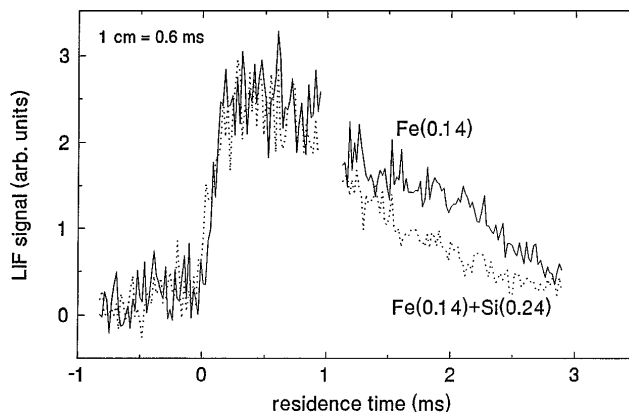


FIG. 9. Centerline profile of FeO(g) concentration as a function of time from the flame front with just iron (case 2) and both iron oxide and silica precursors (case 7).

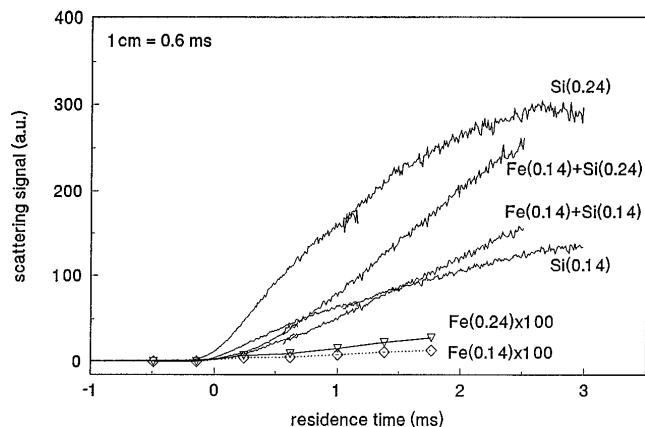


FIG. 10. Centerline scattering profiles for some of the conditions examined. The solid profiles were obtained from the intensified CCD images, and the profiles with discrete points were obtained from separate photomultiplier tube measurements.

precursor (cases 4–5), probably due to the larger size silica particles that are formed. Electron micrographs<sup>16</sup> indicate that the silica particles are on the order of 5 times the size of the iron oxide particles. With particle diameters  $<100$  nm, the scattering signal is close to the Rayleigh regime, and, thus, the scattering signal is proportional to the sixth power of the diameter. Hence, the larger diameter silica particles are expected to show substantially larger scattering signals than the iron oxide particles, and this is borne out in Fig. 10.

Interestingly, for the tests where either silicon or both iron and silicon precursors were added, the scattering profiles initially ( $t < 1.5$  ms) show higher scattering intensities for the single component silica particles than the corresponding nanocomposite, even though iron oxide has a higher refractive index. Farther downstream, however, a crossover in scattering intensity occurs for the low silica loading case, and the trends for the higher silica loading case indicate a similar behavior would occur farther downstream. We believe these results are showing the effects of particle sintering. Helble and Sarofim<sup>37</sup> have estimated sintering times for a number of inorganic aerosols as a function of size and temperature. Based on our measured temperatures, 10 nm silica particles should have a coalescence time of roughly 1–5 ms, which is on the same order as our residence time of about 3 ms. Furthermore, we know that at a 3 ms residence time the nanocomposites are unagglomerated, while showing considerable agglomeration at shorter residence times (based on thermophoretic sampled TEM measurements at several locations within the flame). Iron oxide by contrast has a sintering time of 3 orders of magnitude lower than silica, and one might expect that the nanocomposite would sinter sooner than silica, and thus scatter less light. When both the nanocomposite and silica are sintered, the nanocomposite should show the

enhanced scattering due to the larger molar volume and refractive index.

## V. SUMMARY AND CONCLUSIONS

Planar laser-induced fluorescence and Rayleigh/Mie imaging measurements have been used to examine the mechanisms of particle formation from gas phase species in a flame reactor. During synthesis of ferric-oxide/silica nanocomposites, the relative gas phase precursor  $[\text{FeO}(\text{g})]$  concentration was measured for different feed conditions and compared with particle scattering measurements. The results indicate that the iron oxide particle formation rate is slower than the gas phase precursor decomposition rate, and essentially proceeds after all of the  $\text{FeO}(\text{g})$  has formed. Measurements in flames seeded with both silicon and iron precursors show no significant changes in the rate of formation of  $\text{FeO}(\text{g})$ , indicating that the iron and silicon components nucleate out (form small clusters) independently of each other. Light scattering measurements indicate that sintering effects are faster for the nanocomposite than for silica, in keeping with the known sintering rates for silica and iron oxide.

## ACKNOWLEDGMENT

The authors gratefully acknowledge the assistance of M. I. Aquino during the course of these experiments.

## REFERENCES

1. R. W. Siegel and J. A. Eastman, in *Multicomponent Ultrafine Microstructures*, edited by L. E. McCandlish, D. E. Polk, R. W. Siegel, and B. H. Kear (Mater. Res. Soc. Symp. Proc. **132**, Pittsburgh, PA, 1989), p. 3.
2. R. W. Siegel, Mater. Res. Soc. Bull., October, 60 (1990).
3. A. Pechenik, G. J. Piermarini, and S. C. Danforth, J. Am. Ceram. Soc. **75**, 3283 (1992).
4. R. C. Flagan, H. A. Atwitter, and K. J. Vahala, J. Aerosol Sci. **22**, S31 (1991).
5. A. Gurav, T. Kodas, T. Pluyn, and Y. Xiong, Aerosol Sci. Technol. **19**, 411 (1993).
6. K. Willeke and P. A. Baron, *Aerosol Measurement: Principles, Techniques, and Applications* (Van Nostrand Reinhold, New York, 1993).
7. M. R. Zachariah and R. G. Joklik, J. Appl. Phys. **68**, 311 (1990).
8. A. C. Eckbreth, *Laser Diagnostics for Combustion Temperature and Species* (Abacus Press, Cambridge, MA, 1988).
9. R. K. Marcus, *Glow Discharge Spectroscopies* (Plenum Press, New York, 1993).
10. M. R. Zachariah and D. R. F. Burgess, Jr., J. Aerosol Sci. **25**, 487 (1994).
11. M. R. Zachariah, D. Chin, J. L. Katz, and H. G. Semerjian, Appl. Opt. **28**, 530 (1989).
12. M. R. Zachariah, D. Chin, H. G. Semerjian, and J. L. Katz, Combustion Flame **78**, 287 (1989).
13. H. Chang and P. Biswas, J. Colloid Int. Sci. **153**, 157 (1992).
14. R. K. Hanson, (1986) Twenty-First Symposium (International) on Combustion, p. 1677 (The Combustion Institute, Pittsburgh, PA).

15. R. K. Hanson, J. M. Seitzman, and P. H. Paul, *Appl. Phys. B* **50**, 441 (1990).
16. M. R. Zachariah, M. Aquino, R. Shull, and E. Steel, *Nanostructured Materials*, **5**, 383 (1995).
17. T. T. Kodas, E. Engler, V. Lee, R. Jacowitz, T. H. Baum, K. Roche, S. S. P. Perkin, W. S. Yound, S. Hughes, J. Kedler, and W. Auser, *Appl. Phys. Lett.* **52**, 1622 (1988).
18. N. Toghe, M. Tatsumisago, T. Minami, K. Okuyama, M. Adachi, and Y. Kousaka *Jpn. J. Appl. Phys.* **27**, 292 (1988).
19. P. Biswas, D. Zhou, I. Zitkovsky, C. Blue, and P. Boolchand, *Mater. Lett.* **8**, 233 (1989).
20. M. R. Zachariah and S. Huzarewicz, *J. Mater. Res.* **6**, 264 (1991).
21. D. Zhou, P. Biswas, J. Oostens, and P. Boolchand, *J. Am. Ceram. Soc.* **76**, 678 (1993).
22. H. Chang, W. Y. Lin, and P. Biswas, *Aerosol Sci. Technol.* **22**, 14 (1995).
23. Q. Li, C. M. Sorensen, K. J. Klabunde, and G. C. Hadjipanayis, *Aerosol Sci. Technol.* **19**, 453 (1993).
24. P. Biswas, S. Y. Lin, and P. Boolchand, *J. Aerosol Sci.* **23**, 273 (1992).
25. C. D. Chandler, Q. Powell, M. J. Hampden Smith, and T. T. Kodas, *J. Mater. Chem.* **3**, 775 (1993).
26. R. M. Measures, *Laser Remote Sensing: Fundamentals and Applications* (John Wiley & Sons, New York, 1984).
27. M. Kerker, *The Scattering of Light and Other Electromagnetic Radiation* (Academic Press, New York, 1969).
28. A. S-C. Cheung, A. M. Lyyra, A. J. Merer, and A. W. Taylor, *J. Mol. Spectrosc.* **102**, 224 (1983).
29. S. M. Harris and R. F. Barrow, *J. Molec. Spectros.* **84**, 334 (1980).
30. G. Herzberg, *Molecular Spectra and Molecular Structure, I. Spectra of Diatomic Molecules* (Van Nostrand Reinhold, Co., New York, 1950).
31. A. S-C. Cheung, N. Lee, A. M. Lyyra, A. J. Merer, and A. W. Taylor, *J. Mol. Spectrosc.* **95**, 213 (1982).
32. J. B. Tatum, *Astrophys. J. Supplement* **14**, 21 (1967).
33. B. Lewis and G. von Elbe, *Combustion, Flames and Explosions of Gases* (Academic Press, New York, 1987).
34. M. R. Zachariah and W. Tsang *Aerosol Sci. Technol.* **19**, 499 (1993).
35. M. R. Zachariah and W. Tsang, *J. Phys. Chem.* **99**, 5308 (1995).
36. V. Bedanov, W. Tsang, and M. R. Zachariah, *J. Phys. Chem.* **99**, 11452 (1995).
37. J. J. Helble and A. F. Sarofim, *J. Coll. Int. Sci* **128**, 348 (1989).